INTERFACE SCIENCE 7, 321–338 (1999)


# Extracting Grain Boundary and Surface Energy from Measurement of Triple Junction Geometry

B.L. ADAMS
*Department of Mechanical Engineering, Brigham Young University, Provo, UT, USA*

S. TA'ASAN, D. KINDERLEHRER AND I. LIVSHITS
*Department of Mathematical Sciences, Carnegie Mellon University, Pittsburgh, PA 15213-3890, USA*

D.E. MASON
*Department of Materials Science and Mechanics, Michigan State University, East Lansing, MI 48864, USA*

CHUN-TE WU, W.W. MULLINS, G.S. ROHRER, A.D. ROLLETT AND D.M. SAYLOR
*Materials Science and Engineering Department, Carnegie Mellon University, Pittsburgh, PA 15213-3890, USA*

**Abstract.** Measurement of the geometry of triple junctions between grain boundaries in polycrystalline materials generates large sets of dihedral angles from which maps of the grain boundary energy may be extracted. A preliminary analysis has been performed for a sample of magnesia based on a three-parameter description of grain boundaries. An extended form of orientation imaging microscopy (OIM) was used to measure both triple junction geometry via image analysis in the SEM and local grain orientation via electron back scatter diffraction. Serial sectioning with registry of both in-plane images and successive sections characterizes triple junction tangents from which true dihedral angles are calculated. We apply Herring's relation at each triple junction, based on the assumption of local equilibrium at the junction. By limiting grain boundary character to a (three parameter) specification of misorientation for the preliminary analysis, we can neglect the torque terms and apply the sine law to the three boundaries. This provides two independent relations per triple junction between grain boundary energies and dihedral angles. Discretizing the misorientation and employing multiscale statistical analysis on large data sets allows (relative) grain boundary energy as a function of boundary character to be extracted from triple junction geometry. A similar analysis of thermal grooves allows the anisotropy of the surface energy to be measured in MgO.

**Keywords:** grain boundaries, triple junctions, crystallographic character, grain boundary energy, surface energy, Herring relations

## 1. Background

### *1.a. Motivation*

It is widely accepted that many aspects of materials, from their processing to their properties, depend on the interfaces that they contain. Why focus on two-dimensional defects in particular when point defects and line defects also play such an important role? The answer is that certain phenomena are highly sensitive to the precise structure of interfaces. Heterogeneous precipitation, for example, is one such process: Vaughan demonstrated that variant selection in $\theta'$ precipitation from Al-Cu solid solution at low angle boundaries depended on the crystallography of the boundary [1]. Palumbo and others have shown how processing lead

for battery electrodes to have a high fraction of special boundaries results in greatly enhanced electrode life [2]. Whether or not microstructural evolution occurs as a uniform, homogeneous process, it is highly sensitive to boundary properties. Abnormal grain growth, for example, can occur if there are large variations in boundary mobility and energy [3]. These considerations and many others provide the motivation for a broadly based investigation into the properties of interfaces.

### *1.b. Aim and Approach*

The aim of this paper is to lay out a procedure for measuring the properties of interfaces as a function of their crystallographic character. The scope is limited to determination of excess free energy of homophase interfaces, i.e. grain boundaries in single phase materials. The approach relies on measurement of the geometry and crystallography of grain boundary junctions i.e. triple points [4], Fig. 1. Specifically, the crystallographic orientations of each grain, the grain boundary tangents and the triple line tangent are measured with the aid of serial sectioning. The analytical procedure for extracting energies is statistical and multiscale which means that the number of measurements must be large enough to ensure that each boundary type has been adequately sampled. It is assumed that local equilibrium exists at each triple junction so that the Herring relations (for force balance) may be applied

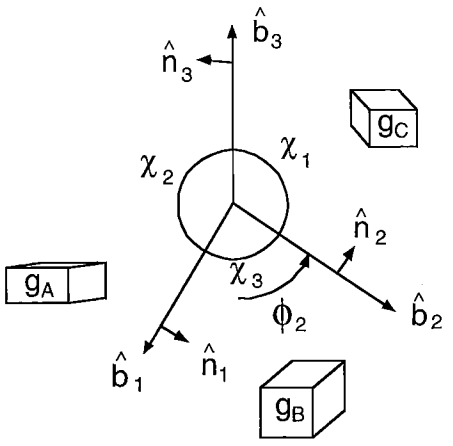


*Figure 1.* Diagram of a labeling convention for grain boundary character, showing dihedral angles, $\chi$, inclination angles, $\phi$, boundary tangent vectors, **b**, boundary normals, **n**, and grain orientations, $g$. The triple junction line is perpendicular to the plane of the diagram.

[5]; a possible limitation of this assumption is discussed in Section 2.b.ii. Each triple junction provides two independent relations between boundary energies. Analysis of the set of relations generates a distribution of boundary energies that (simultaneously) satisfies the Herring relations at each triple junction. A caveat on the application of Herring's relations as equalities is noted in Section 2.b.i.

The current size of the data sets is only large enough, however, to allow for the analysis to be executed on the basis of a three-parameter description of grain boundary character. The results for measurements in magnesia indicate that the conventional view of uniform boundary energy except for low angle boundaries and for well matched lattices, as indicated by a high fraction of coincident sites (low sigma value) is not likely to be true. For a special case of grain boundaries in equilibrium with solid-vapor surfaces in MgO for which one of the torque terms could be neglected, a reconstruction of the *surface energy* has been performed that includes torque terms for the solid-vapor surfaces. The results from this analysis indicate that the torque terms are very important for determination of the map of surface energy. Torque terms arising from the inclination dependence of the boundary energy for internal triple junctions (i.e. between three grain boundaries) will be included in the analysis of (five parameter) grain boundary energy once larger data sets are available.

### *1.c. Current Knowledge of Grain Boundary Energy*

Current knowledge of the properties of grain boundaries is limited to special boundary types. Furthermore much of the available literature concerns computer simulation. Thorough reviews by Wolf and Yip and, more recently by Sutton and Baluffi [6] provide excellent overviews of boundary structure and properties. Most experimental determinations of grain boundary energy have relied on a knowledge of surface energy, e.g. [7]. Almost the only work on oxides is that of Dhalenne et al. who measured thermal grooves on NiO for boundaries in ⟨110⟩ tilt boundaries [8]. Their results indicated little variation in energy for ⟨100⟩ high angle tilt boundaries. ⟨110⟩ tilt boundaries, however, showed cusps at the $\Sigma 9$ (221 plane), $\Sigma 11$ (311 plane) and the (expected) $\Sigma 3$ positions. The grain boundary energies were higher for ⟨110⟩ misorientations than for ⟨100⟩ boundaries, although this result assumed constant surface energy.

As discussed elsewhere, surface energy is found to be orientation (inclination) dependent in another ceramic, MgO. More recently Otsuki [9, 10] has conducted a series of experiments on aluminum in which intersections of grain boundaries with a solid-liquid surface were characterized. By assuming a constant solid-liquid interfacial energy and examining a variety of interfaces based on ⟨100⟩ and ⟨110⟩ rotation axes, information has been obtained on symmetric tilt, asymmetric tilt, twist and mixed character boundaries. The results also showed cusps at the $\Sigma 11$ (311 plane) and the (expected) $\Sigma 3$ positions, though not at the $\Sigma 9$ (221 plane) position. Their results also confirmed previous results for metals, i.e. that twist boundaries tend to have lower energies than the corresponding tilt boundaries. A concern with this approach is that a concentrated alloy is used as the liquid in order to avoid melting the (unalloyed) solid aluminum: solute will diffuse into the solid, especially along boundaries and the presence of the solute may perturb the boundary energy.

## 2. Theory

The treatment of grain boundaries (surfaces) presented here is limited to thermodynamic level. The atomic structure of interfaces is unquestionably essential to understanding their structure and properties. The aim here is, however, to develop a characterization that is complete with respect to the geometric variables. In general we expect the properties of interfaces to be dependent on their crystallographic character. The particular property of interest in this case is the excess free energy, commonly referred to as grain boundary energy or surface energy, $\sigma$:

$$\sigma = \left[\frac{\partial E}{\partial A}\right]_{S,V,N_i}$$

The boundary energy is the increase in the internal energy, $E$, per unit increase in boundary area, $A$, holding entropy, $S$, volume, $V$, and components, $N_i$, constant. The boundary energy thus depends on a large number of thermodynamic variables including temperature, pressure, chemical potential of the various components in the system and the geometric variables that define crystallographic character, to be discussed below. The property of boundary energy can be measured in an experiment in which creation or annihilation of boundary area is balanced against a force or stress. Zero creep experiments in bamboo structured wires represent one such example. Triple junctions represent another example in which a force balance establishes a local equilibrium so that their geometry is a measure of (relative) boundary energies. Before describing the crystallography of boundaries we review some key aspects of (local) equilibrium at triple junctions. The following section assumes a dependence of boundary energy on inclination whose crystallographic nature is implied.

### 2.a. *Herring Relations*

Herring equations [11], describing equilibrium at a triple junction, result from the requirement that a virtual displacement of the triple junction in any direction causes no first order change in energy. The equations are

$$\sum_{j=1}^{3}\{\sigma_j \hat{b}_j + (\partial\sigma_j/\partial\phi_j)\hat{n}_j\} = \vec{0} \qquad (2.1)$$

where the sum is conducted over the three interfaces intersecting at the triple junction, $\sigma_j$ is the excess free energy of the $j$th boundary, $\hat{n}_j$ is the unit boundary normal of the $j$th boundary, $\hat{b}_j$ is a unit vector lying in the $j$th boundary and perpendicular to the triple line, $\hat{l} = \hat{n}_j \otimes \hat{b}_j$, which is common to all three adjacent boundaries and $\phi_i$ is defined to be the right handed angle of rotation about $\hat{l}$ of the $j$th boundary from a reference direction. The derivative terms are referred to as torque terms and reflect the dependence of interface energy on orientation about the triple junction at fixed $\hat{l}$.

If the interface energy is independent of interface orientation, Herring's equations reduce to the Young equations

$$\frac{\sigma_1}{\sin(\chi_1)} = \frac{\sigma_2}{\sin(\chi_2)} = \frac{\sigma_3}{\sin(\chi_3)} \qquad (2.2)$$

### 2.b. *Limitations on Herring Relations*

The standard form for the Herring Relations quoted above shows an equality. For inclinations of one or more grain boundaries corresponding to an energy cusp (with respect to inclination), some of Herring's relations may become inequalities. Qualitatively, this results in a situation in which boundaries intersecting the cusp boundary may occupy a range of angles, all of which satisfy the conditions of equilibrium.

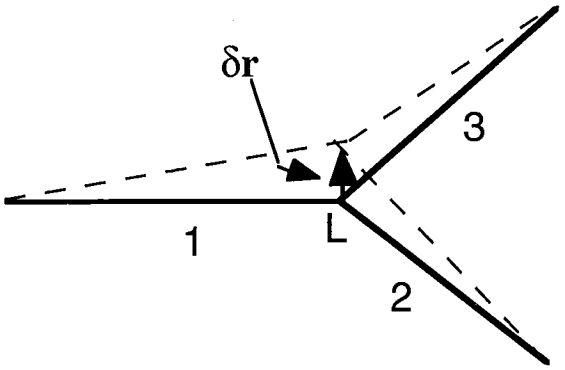


*Figure 2.* A virtual displacement of the intersection line $L$ of three interfaces. The condition for equilibrium is $\delta E \leq 0$, where $E$ is the free energy (see text). Herring's equations result if and only if $\delta E = 0$.

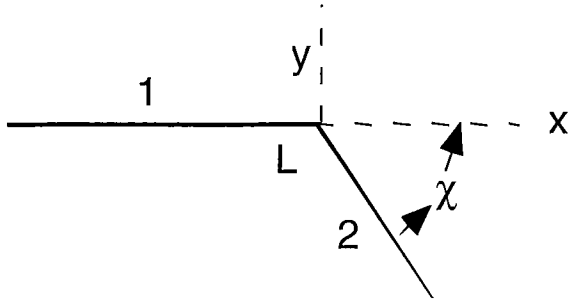


*Figure 3.* Interface 1 is in a steep cusp orientation such an $x$ displacement of $L$ gives $\delta E = 0$ but a vertical displacement gives $\delta E \geq 0$. The corresponding results are the equality $\sigma_1 = \sigma_2 \cos\chi$ and the inequality $\sigma_2 < -(\partial\sigma/\partial\phi)_-$.

***2.b.i. Conditions Under which Some Herring Equations for Intersecting Interfaces Become Inequalities.*** Consider three interfaces intersecting along a line $L$. Let $\delta E$ be the change in free energy to first order corresponding to a virtual displacement $\delta\vec{r}$ of the intersection line as shown in Fig. 2. The condition for equilibrium [12] for an isothermal system at constant volume [13] is that $\delta E \geq 0$ for all $\delta\vec{r}$. If $\delta E = 0$ for all $\delta\vec{r}$, then Herring's equations follow [11]. If the orientation of one or more interfaces corresponds to a steep energy cusp, however, it is quite possible for the sharp inequality $\delta E > 0$ to hold for some displacements $\delta\vec{r}$. In these cases, some of Herring's equations are replaced by inequalities that contain the values $(\partial\sigma/\partial\phi)_-$ or $(\partial\sigma/\partial\phi)_+$ of the interfaces in cusps, where $(\partial\sigma/\partial\phi)_- < 0$ is the increase in $\sigma$ upon twisting an interface out of the cusp orientation by the angle $\phi$ in the negative angular sense (clockwise) and $(\partial\sigma/\partial\phi)_+ > 0$ is the increase in $\sigma$ upon twisting the interface in the positive angular direction. The inequalities can be written as Herring equalities only if artificial values of the angular derivatives $\partial\sigma/\partial\phi$ are chosen [14] that lie between the true cusp values.

The simplest illustration of the $\delta E > 0$ case is shown in Fig. 3 which depicts two straight segments, 1 and 2, of an interface intersecting at $L$. For simplicity, segment 1 along the $x$ axis is assumed to lie in a steep cusp orientation with a free energy $\sigma_1$ and cusp derivatives $(\partial\sigma/\partial\phi)_-$ and $(\partial\sigma/\partial\phi)_+$ of large magnitude whereas segment 2 is assumed to have a free energy $\sigma_2$, with a negligible orientation dependence over the range of angles near the one shown. A displacement in the $x$ direction allows $\delta E = 0$ with $\sigma_1 = \sigma_2 \cos\theta$, but a displacement in the negative $y$ direction gives the inequality (by assumption) $\delta E > 0$ with the conclusion $\sigma_2 \sin\theta < (\partial\sigma/\partial\phi)_-$; that is, the vertical resolved force exerted by segment 2 is insufficient to twist segment 1 out of the cusp. If a Herring equation is forced, an artificial value of $\partial\sigma_1/\partial\phi$ given by $\sigma_2 \sin\theta = -\partial\sigma_1/\partial\phi > (\partial\sigma/\partial\phi)_-$ will be deduced. Segments 1 and 2 can be imagined to comprise a portion of the Wulff form of a crystal of constant volume embedded in a second crystal. Then the situation described above can be shown to occur if the $\sigma$ plot lies outside the pedal of the Wulff form (except at cusps).

For triple junctions, the Herring equations (resulting from $\delta E = 0$) uniquely determine the equilibrium dihedral angles of intersection. If $\delta E > 0$ holds, however, there will generally be a range of possible equilibrium dihedral angles for three given interfaces. This is easily seen by adding a third interface to Fig. 3 to yield Fig. 4, still assuming interface 1 to lie in a steep cusp and interfaces 2 and 3 to be isotropic. Then any combination of angles that gives the balance of forces resolved along $x$, $\sigma_1 = \sigma_2 \cos\theta_2 + \sigma_3 \cos\theta_3$ (assuming $\sigma_1 \leq \sigma_2 + \sigma_3$) will result in equilibrium as long as the forces of interfaces 2 and 3 resolved along $y$ are insufficient to twist interface 1 out of the cusp. If the Herring equations are blindly applied to sets of triple junctions in this range, a corresponding range of artificial $\partial\sigma/\partial\phi$ values, which all lie between $(\partial\sigma/\partial\phi)_-$ and $(\partial\sigma/\partial\phi)_+$, will be ascribed to 1.

If any interface cusps exist that are sufficiently steep to give rise to the inequalities described above, it is expected that they will be revealed by a range of values of $\partial\sigma/\partial\phi$ that must be ascribed to the corresponding interface in order to satisfy Herring's equations.

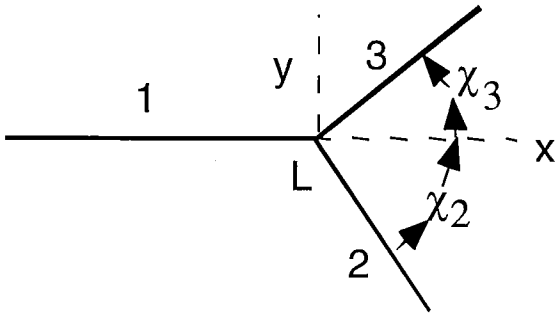


*Figure 4.* Again interface 1 is in a steep cusp orientation such that a range of equilibrium angles $\chi_2$ and $\chi_3$ are possible where $\sigma_1 = \sigma_2 \cos\chi_2 + \sigma_3 \cos\chi_3$. In this range, the resolved vertical tensions of interfaces 2 and 3 are assumed insufficient to twist interface 1 out of the cusp orientation.

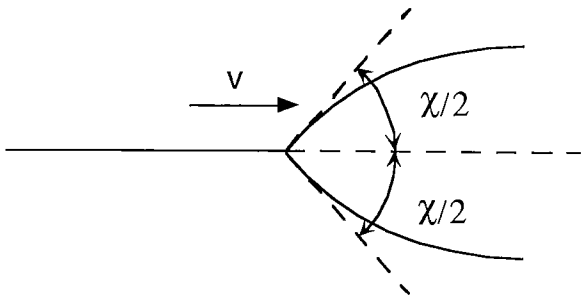


*Figure 5.* A moving vertex of three intersecting boundaries with a dihedral angle $\chi$ between moving curved grain boundaries. $\chi$ may deviate from the equilibrium value in order to supply the force necessary to move the vertex.

A final technical point is that Herring's equations say nothing about stability; they describe both stable and unstable equilibrium of intersecting interfaces. The latter, however, would not be expected to be observable. Further, a curvature driven evolving system with the Herring relations satisfied on triple lines is dissipative and its stationary configurations have stability properties.

***2.b.ii. The Effect of Triple Junction Drag on Grain Boundary Intersection Angles.*** If there is a significant force per unit length $f_V$ required to move a vertex or triple junction of intersecting grain boundaries because of a low intrinsic mobility, or perhaps because of a the drag of a solute cloud, the dihedral angles of intersection of the grain boundaries can differ appreciably from their equilibrium values. Rather than the zero resultant force at the vertex characteristic of equilibrium, there must be a sufficient resolved force to move the vertex in concert with the attached grain boundaries. The effect has been discussed by Fradkov and Udler [15]. The deviation of the intersection angles from their equilibrium values decreases with increasing grain size because less force is required to keep the vertex moving together with the slower moving grain boundaries.

An estimate of the deviation of intersection angles due to vertex drag can be made as follows: consider the vertex shown in Fig. 5 moving along the positive $x$ axis with symmetric two dimensional boundaries of radius of curvature $R$ and a dihedral angle $\chi$. All boundaries are assumed to have the same free energy $\sigma$. The velocity $v$ of the vertex required by the boundary motion will be $v = m_B \sigma \sin(\chi/2)/R$, where $m_B$ is the boundary mobility, and $\sigma/R$ is the driving force for boundary motion. This velocity requires a driving force on the vertex of $f_V = v/m_V = m_B\sigma \sin(\chi/2)/m_V R$ where $m_V$ is the vertex mobility. The driving force is supplied by the resolved force in the $x$ direction of $f_V = \sigma(2\cos(\chi/2) - 1)$. Equating forces gives

$$\frac{2\cos(\chi/2) - 1}{\sin(\chi/2)} = \frac{m_B}{m_V R} = \frac{m_B^a a}{m_V^a R} \equiv \rho \qquad (2.3)$$

where in the next to the last member of the equation, $a$ is an atomic dimension and $m_B^a$ and $m_V^a$ are respectively atomic mobilities in the two cases, that is, $v = m_B^a f_a$ and $v = m_V^a f_a$ where $f_a$ are the forces per atom; the last member simply defines the dimensionless parameter $\rho$.

In pure materials, it is reasonable to expect the atomic mobilities to be usually comparable in the boundary and in the vertex. Then Eq. (2.3) shows that for grain sizes appreciably larger than atomic dimensions, that is, for $a/R \ll 1$, the left hand side gives essentially $\chi \approx 120°$, the equilibrium value. More precisely, if $\rho \ll 1$, and if $\delta = 120 - \chi$ is the deviation of the dihedral angle from the equilibrium value, then Eq. (2.3) shows that $\delta \approx \rho$. Note that the deviation becomes smaller the larger the grain size (and hence the smaller $\rho$). Hence under these conditions, dihedral intersection angles at moving vertices are not expected to deviate significantly from their equilibrium values.

If there is an appreciable solute drag effect, however, $\rho$ may not be small compared to unity for small grains. Eq. (2.3) may then be solved for the steady-state dihedral angle. In principle, departures from the equilibrium dihedral angles in experimental data would be revealed if vertices of a given crystallographic type

showed variations in the dihedral intersection angles depending on scale and the movement of the vertices.

## 3.

### *3.a. Geometric Variables: Misorientation*

Disregarding atomic translational degrees of freedom, five degrees of freedom exist for internal boundaries (two for surfaces) since three are associated with the relationship between the crystal lattices and two more with the (angular) position of the boundary plane, i.e. the inclination, Fig. 1. These five degrees of freedom may parameterized in a number of different ways. Even for the lattice misorientation itself, commonly notated as $\Delta g$, there are descriptions based on (orthogonal) matrices, axis-angle pairs, Euler angles, quaternions and Rodrigues vectors. Inclination, commonly notated as $\hat{n}$ for the unit vector representing the outward pointing normal, has descriptions based on Miller indices and polar angles. As might be expected from the wide range of phenomena in which grain boundary character plays a role, each of these descriptions has been used to emphasize particular aspects of boundary character. The physical metallurgy literature has tended to favor lattice misorientation and to neglect boundary inclination especially in the area of grain boundary engineering [2]. The literature on boundary structure has tended to emphasize boundary plane and consider only a limited range of highly symmetric lattice misorientations [16].

For numerical calculations, misorientation is conveniently described by a nine element orthogonal matrix, $\Delta g$. When the orientations of the two adjoining crystals are obtainable also as rotation matrices, $g_A$ and $g_B$, then the misorientation is the product of the one with the transpose of the other; $\Delta g = g_B g_A^T$, the order depending on which crystal is chosen as reference. The matrix form can related to an axis-angle representation by the following, where $\theta$ is the rotation angle, or misorientation angle, and $(u, v, w)$ is the axis written as a unit vector, i.e. $u^2 + v^2 + w^2 = 1$, see p. 68 et seq. in [17] for a summary of this and other parameterizations mentioned here. Although misorientation is a three-parameter quantity, it is sometimes sufficient to consider use the misorientation angle, $\theta$. as a one-parameter description. This simplification is useful for distinguishing between low-angle and high-angle boundaries.

Quaternions are related to the axis-angle description by specification of a four dimensional vector, $Q : Q = (u \sin\theta/2, v \sin\theta/2, w \sin\theta/2, \cos\theta/2)$. The symmetry elements of the cubic point groups take on a simple form as quaternions which is useful for certain numerical procedures. The Rodrigues vector, $R$ (or $\rho$ in some texts) is related to the axis vector in a similar way but its length is specified by the semi-angle tangent.

$$R = (R_1, R_2, R_3) = \tan(\theta/2)(u, v, w)$$

Misorientation can also be parameterized with three Euler angles, $\phi_1$, $\Phi$, and $\phi_2$, that represent the sequence of rotations required to bring the two crystals into coincidence. The same set of parameters is in common use for orientations $(g)$. By way of an approximate analogy, a pilot knows these angles as pitch, yaw and roll. Interconversion formulae can be found in the standard texts [18] and the following example shows how to obtain the transformation matrix from the Euler angles.

$$\Delta g(\phi_1, \Phi, \phi_2) = \begin{pmatrix} \cos\varphi_1 \cos\varphi_2 - \sin\varphi_1 \sin\phi_2 \cos\Phi & \sin\varphi_1 \cos\varphi_2 + \cos\varphi_1 \sin\varphi_2 \cos\Phi & \sin\varphi_2 \sin\Phi \\ -\cos\varphi_1 \sin\varphi_2 - \sin\varphi_1 \cos\varphi_2 \cos\Phi & -\sin\varphi_1 \sin\varphi_2 + \cos\varphi_1 \cos\varphi_2 \cos\Phi & \cos\varphi_2 \sin\Phi \\ \sin\varphi_1 \sin\Phi & -\cos\varphi_1 \sin\Phi & \cos\Phi \end{pmatrix}.$$

Symmetry elements of the crystal structure are applied to each of the two orientations to bring the misorientation into the fundamental zone, i.e. the set of all the physically distinguishable boundary types (without repetition), see e.g. p. 12–17 in [6]. This procedure also minimizes the associated misorientation angle $(\theta)$ and the result is known as the disorientation in order to distinguish it from general misorientations [16]. In Rodrigues-Frank space [19, 20] reduced by the symmetry of cubic-cubic symmetry applicable to grain boundaries, the three components have the range $0 \leq R_1 \leq (\sqrt{2} - 1)$, $0 \leq R_2 \leq R_1 \leq (\sqrt{2} - 1)$, and $0 \leq R_3 \leq R_2 \leq (1/3)$." The shape of the fundamental zone is a truncated pyramid which by convention is represented as a series of triangular sections each taken at constant $R_3$. A common further simplification reduces the misorientation to a sorting by coincidence site boundary type, which is defined by the sigma number [21, 22]. This analysis is based on finding the set of discrete

misorientations for which a finite fraction of the lattice points in one crystal are exactly coincident with lattice points in the second crystal, based on an imaginary overlap of the two lattices [23]. The twin boundary, for example, based on a 60° rotation about ⟨111⟩ leads to one site in three coincident between the two lattices, written as Σ3. Transmission electron microscopy permits a more detailed view of boundaries and so there has been more effort to characterize the inclination as well as the lattice misorientation with this technique.

### 3.b. *Geometric Variables: Inclination*

***3.b.i. Misorientation Based.*** A complete crystallographic characterization is obtained by extending the three parameter description of lattice misorientation to include two more parameters for the boundary inclination, conventionally notated by the pair $(\Delta g, \hat{n})$. A convention is needed for which of the two adjoining lattices is used to describe the boundary normal. Referring to Fig. 1, we adopt the outward pointing normal for the first grain proceeding anticlockwise around the triple line tangent. The inclination can be parameterized by either Miller indices, preferably reduced to unit vectors, or as a pair of spherical angles; (solid-vapor) surface normals can also be parameterized in this way. Given a boundary normal measured in the specimen frame, $\hat{n}_s$, the normal referred to the first crystal is $\hat{n}_A = g_A \hat{n}_s$. If a conventional fundamental zone is adopted for the misorientation such as the truncated pyramid appropriate to Rodrigues vectors, then a full hemisphere is required for the inclination $(-1 \leq h \leq +1, -1 \leq k \leq +1, 0 \leq l \leq +1)$ because specific symmetry operators were identified in order to place the misorientation in its fundamental zone.

Three reservations must be mentioned concerning this approach to a five parameter description of grain boundary character. First, the choice of one grain over the other for the boundary plane is somewhat arbitrary, especially in view of the fact that internal boundaries are best understood as a pair of free surfaces. Second, any special character based on tilt or twist character in the boundary is obscured by this choice of parameters. That is to say, any special relationship between the inclination and the misorientation axis is not readily apparent in this representation. Lastly, this parameterization of a boundary places primary emphasis on the relationship between the two lattices adjoining the boundary.

***3.b.ii. Tilt-Twist Decomposition.*** If one regards a grain boundary as the joining of two surfaces, the natural description of boundary character is in terms of its tilt and/or twist character. This approach has long been known for small angle boundaries but is equally applicable to high angle boundaries. There is not space to provide a complete review: see, for example, Sutton and Baluffi [6]. Wolf has demonstrated that the lattice misorientation at any boundary may be described by a combination of tilt and twist rotations [24]. The relationship between the boundary normals for the two surfaces comprising the boundary is given by the tilt rotation and the remaining parameter is the twist rotation about the boundary normal. Most grain boundary simulations are based on special relationships such as symmetric twin boundaries [25]. This results in a five parameter description of the form $(\hat{n}_A, \hat{n}_B, \phi)$, where $\hat{n}_A$ and $\hat{n}_B$ are boundary normals referred to the crystal lattices on either side of the boundary $(\hat{n}_A = g_A \hat{n}_s, \hat{n}_B = g_B \hat{n}_s)$ and $\phi$ is the twist angle between the lattices. Each boundary normal requires two parameters as described above. The fundamental zone includes the 001-101-111 triangle for the the first boundary, the 001-110-111-011 quadrant for the second boundary and $0 \leq \phi \leq 2\pi$. One caution concerning this approach is that although it has been stated that a symmetric tilt boundary is equivalent to a 180° twist, this is only valid for boundary plane normals that lie on a mirror plane of the crystal symmetry. Also low angle boundaries are not immediately apparent in this parameterization except as similar boundary planes with small twist angles.

### 3.c. *Justification of Mesoscale Approach*

Regardless of the choice of parameterization of geometric variables, it is clear that determination of grain boundary properties over the complete fundamental zone requires a large number of data points. For a two degree resolution in a discretized space in which each parameter ranges from typically zero to 45°, the number of points is of order five million, i.e. $(45°/2°)^5$. The available resolution will therefore depend entirely on the size of the data set that can be accumulated. A two degree resolution is, however, close to the minimum that is required in order to define local minima in grain boundary energy, for example, as is the case for the Σ3 twin. Cusps at coincident site lattice positions are expected to be on the order of $15°(\Sigma)^{-1/2}$ [21] which

means 7° for $\Sigma 5$, 6° for $\Sigma 7$ and so on. Therefore reconstructing the variation in grain boundary energy over the fundamental zone of five geometric variables in cubic materials is a challenging task. Detailed characterization of the atomic structure of individual boundaries is impracticable and therefore a mesoscopic approach is required.

### *3.d. Statistical/Multiscale Analysis*

A grain boundary network in a single phase material contains a set of triple junctions that, in the absence of drag effects discussed above, may be taken to be each in local equilibrium. The grain boundary energy map is the solution of a large system of differential equations satisfying certain boundary conditions on the triple lines. Solving this system by studying the boundary conditions is a relatively unstable process. The data requires consideration of a large disparate and inconsistent data set that provides only the coefficients of equations satisfied by the solution rather than an unbiased estimator of the solution. From these points of view, this is a rather unusual problem, one for which we have not yet found an analogue in the literature. The method described below to infer the excess free energy of grain boundaries from triple line data is found to be robust and flexible. It produces a table of values for the energy function which may then be fit to any desired representation, for example, a Fourier Series or spherical harmonics.

***3.d.i. Method for Grain Boundary Energy Reconstruction.*** In general, the grain boundary energy depends on the five crystallographic degrees of freedom. To illustrate the method, consider a simplified case in which an equilibrium columnar structure consists of a planar network of curves meeting at triple points, effectively reducing the number of degrees of freedom to two. The excess free energy of each arc $\Gamma$ is given by a non-negative function $\sigma(\phi, \theta)$, where $\phi$ is the angle measured from a reference direction that describes the inclination of each boundary and $\theta$ is the misorientation angle between the lattices, usually taken to be the minimum or disorientation angle:

$$\begin{aligned}\sigma(\phi,\theta),\ \hat{n} &= (\cos\phi, \sin\phi) \text{ the normal of } \Gamma,\\ \hat{b} &= (\sin\phi, -\cos\phi) \text{ the tangent of } \Gamma,\\ \theta &= \text{the lattice misorientation across } \Gamma.\end{aligned}$$

At three arcs $\Gamma^{(1)}, \Gamma^{(2)}, \Gamma^{(3)}$ separating three grains meeting at a triple junction $p$, equilibrium equations are assumed to hold on the $\Gamma^{(j)}$ and the Herring condition

$$\sum_j \left( \frac{d\sigma}{d\phi}(\phi^{(j)}, \theta^{(j)})\hat{n}^{(j)} + \sigma(\phi^{(j)}, \theta^{(j)})\hat{b}^{(j)} \right) = 0 \text{ at } p. \tag{3.4}$$

The interrogation of the sample yields values of a discrete set of the independent variables $(\phi, \theta)$ and the geometric coefficients $(\hat{n}, \hat{b})$ occuring in a given system of equations of type (3.4). Our objective is to use this information to tabulate the values of $\sigma(\phi, \theta)$ for this discrete set.

***3.d.ii. Discretization.*** To begin, select a level of discretization, $M$, for $(\phi, \theta)$ and consider the normal angle interval $[0, \pi]$ and the lattice misorientation angle interval $[0, \frac{1}{2}\pi]$ divided into $M$ subintervals. More precisely, in order to handle the torque terms in an efficient way, the $\phi_i$'s are taken to be defined at the end points of the intervals and the $\theta_j$'s at the centers of the intervals, a staggered discretization. The discretized Eq. (2.4) has the form, $h = \pi/M$,

$$\begin{aligned}\sum_k \frac{1}{h}\left(\sigma\left(\phi_{i_k} + \frac{1}{2}h, \theta_{j_k}\right) - \sigma\left(\phi_{i_k} - \frac{1}{2}h, \theta_{j_k}\right)\right)n^{(k)}\\ + \frac{1}{2}\left(\sigma\left(\phi_{i_k} + \frac{1}{2}h, \theta_{j_k}\right) + \sigma\left(\phi_{i_k} - \frac{1}{2}h, \theta_{j_k}\right)\right)b^{(k)} = 0\end{aligned} \tag{3.5}$$

For a given triple junction, $p$, there are two independent values of $\phi$ and two independent values of $\theta$ since, for the columnar structure considered here,

$$\sum \phi_{i_k} = 2\pi \quad \text{and} \quad \sum \theta_{i_k} = 0.$$

The resulting pair of independent values, $(\phi, \theta)$, fit into a pair of such intervals. We may in this way determine an urn corresponding to equations whose $(\phi, \theta)$ pairs sort into a pair of given intervals. There are $N = \binom{M}{2} \times \binom{M}{2}$ such urns. The statistical step of our method is to assume that each assignment of an equation into a given

urn is an independent trial and to replace the equations that eventually occur in a given urn by the equation with the average coefficients. According to the Law of Large Numbers, the average of the coefficients is the most probable value. Let us write $M = 2^L$ and call $L$ the *level*. The result is a system of $N$ equations in $2M$ unknowns that may be expressed as

$$A_{(L)}x_{(L)} = 0. \tag{3.6}$$

There are situations, especially when the data set is small, when inspection of the statistics of the individual urns allows us to disregard outlying members. How this may be related to equilibrium of the triple junctions is an issue we shall address in a later article. $N$ is generally small relative to the size of the data set.

***3.d.iii. Multiscale Procedure.*** The multiscale step in the method is organized in this way. Choose $L = 2$ and solve the system represented by Eq. (3.6) for $x_{(2)}$. Next choose $L = 3$, sort the data into new urns and apply the statistical step and then, with $x_{(2)}$ as the initial approximant, find $x_{(3)}$. This process of increasing the discretization is the heart of the multiscale technique: the level of discretization is increased, the data is sorted and averaged, and the system, Eq. (3.6), is solved using the prior coarse solution as the starting trial. A Kaczmarz technique, which corresponds to an iterative projection method, is employed to resolve the system at each level. System (3.6) does not, in general, admit a unique solution, i.e., it is not solved in the mathematical sense. However implementing several Kaczmarz relaxations on each level of discretization allows us to obtain an optimal approximation $x_{(L)}$ which serves as a good approximation to begin computing $x_{(L+1)}$.

There are several criteria for ending the process. Two reasonable criteria are, (a), when almost all the urns are very sparsely populated and, (b), by consideration of the residual of 3.6. The choice of the urns, their sizes and distribution, is determined adaptively during the solution process as the discretization is refined. Regions with more data end up with more urns of smaller size. Thus the reconstruction is adapted to the data available in a given experiment. Moreover, the multiscale approach allows for a natural treatment of noisy data by comparing the solutions obtained at different levels of discretization, i.e., different values of $L$. As long as the successive differences in the solution decrease, further refinement is performed. When noise begins to dominate, these differences no longer decrease, giving a natural stopping criterion.

## 4. Experimental Method

### *4.a. Mesoscale Interface Mapping System (MIMS)*

Recovery of the energy function from the mesostructure of the polycrystal requires a precise three dimensional characterization of the geometry and crystallography of the grain structure. These requirements are not satisfied in conventional characterization, and so new methods have had to be developed. The mesoscale interface mapping system (MIMS) described below has been specifically developed for the recovery of energy distributions from microstructure.

The *idealized aggregate function* $G(x)$ [1] provides a sufficient representation of the mesostructure:

$$G(x) = \{\phi(x), g(x)\}. \tag{4.1}$$

Here $\phi$ and $g$ denote the crystalline phase and orientation, respectively, as a function of position in the material. It should be evident that, as defined, $G(x)$ carries information about the size, shape and arrangement of grains, their phases, their crystallographic orientations, and their interconnectivity via the system of grain boundaries and triple junctions.

Orientation imaging microscopy (OIM) [26], permits rapid characterization of $G(x)$ in the two-dimensional section plane. OIM comprises stepping with the electron beam of a scanning electron microscope (SEM) over a regular grid of points $\{x\}$ restricted to the section plane ($x \in \mathcal{R}^2$), and capturing and indexing the electron back-scattered patterns (EBSPs) for the phase and orientation at each grid point. The spacing of grid points is governed by the spatial resolution required for $G(x)$.

For the present application, the distribution of interfaces and triple junctions by type and character is of primary interest. For these applications OIM is rather inefficient since only the scan points that lie adjacent to the interfaces are used to determine interface and triple junction character. Furthermore, a complete mesoscale characterization requires sampling the three-dimensional aggregate function $G(x)$ ($x \in \mathcal{R}^3$) which entails serial sectioning with OIM. That is, the size of the data set in the conventional approach scales with the cube of the linear dimension of the

characterization region, whereas it should scale as the square or less.

MIMS overcomes the challenges associated with conventional OIM. The efficiency of sampling the microstructure for lattice orientation only as needed near interfaces is realised by directing the beam to the vicinity of interfaces which have been identified by a microstructural contrast image. This also enables sufficient sampling near the interface to establish in-plane inclination with sufficient angular resolution. The need for 3-dimensional characterization of boundaries is met by a system of algorithms for achieving a precise spatial registry between adjacent microstructural data sets. Here the principal experimental challenge is to achieve a high degree of parallelism between adjacent section planes, and an accurate registry between the two-dimensional $G(x)$ data.

Figure 6 shows the basic structure of the MIMS as it is applied to each individual scanned sector on the section plane. A sector is defined as a 2-dimensional region of breadth specified by the operator of the system but typically containing a few grains. Its dimension is selected such that individual boundaries in the section plane are characterized with sufficient angular resolution by the microscope. When characterization of a wide field in the section plane is desirable, data upon several (overlapping) sectors is taken. These overlapping data sets can subsequently be "stitched" together ("in-plane registration") in order to form a wide field (2-dimensional) mosaic of the microstructure.

For the characterization of each 2-dimensional sector, three functional modules and a central control system are employed as illustrated in Fig. 7:

(1) Microscope: digital scanning electron microscope with appropriate detectors for contrast formation and for recording EBSPs.
(2) Image Processing: used for morphological and geometrical processing of scanning contrast images.

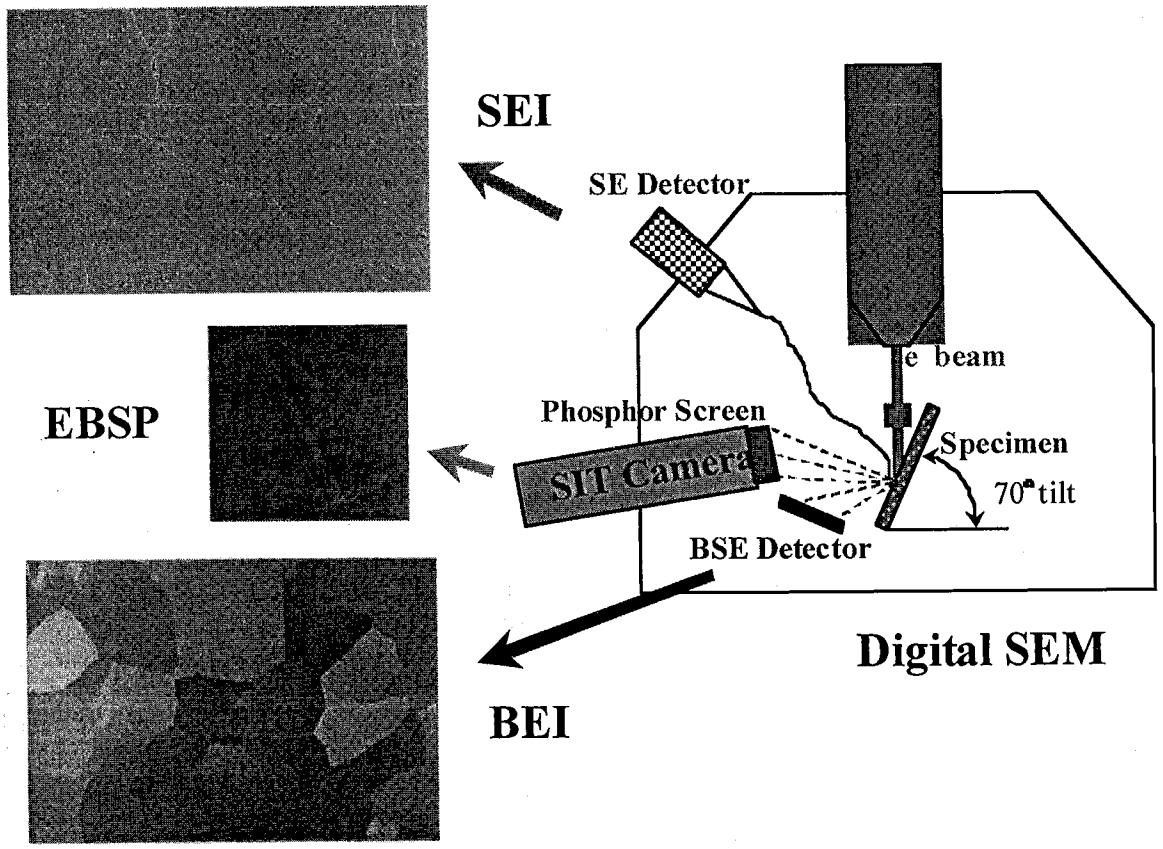


*Figure 6.* A typical configuration of a digital SEM. When used in scanning mode, back-scattering electron images (BEI) or secondary electron images (SEI) are produced. When used in spot mode, EBSP images are formed.

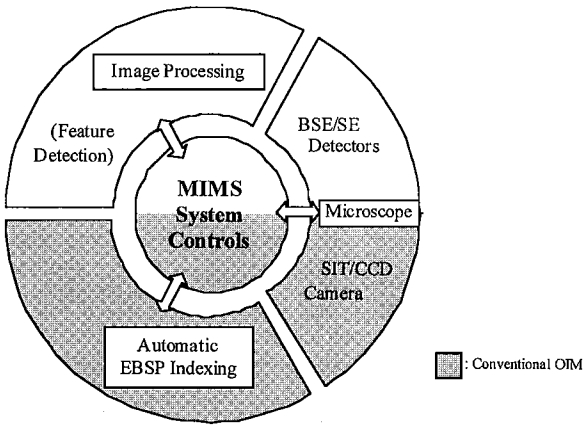


*Figure 7.* Schematic diagram of MIMS system showing relationship between the major components.

(3) Automatic EBSP Indexing: used for automated lattice orientation determination.
(4) Systems Control: used to sequence the operations of the aforementioned modules, information transfer, and output.

Figure 7 also highlights the differences between conventional OIM and the 2-dimensional MIMS technology.

### *4.b. Image Processing*

MIMS differs from OIM in its use of a second detector system in conjunction with the SEM to form contrast images of the microstructure in the sector. This second detector system is used to form intensity contrast images. One or more detectors might be involved in the system as required to obtain adequate contrast using the conventional SEM scan mode. Typical detectors employed sample the back-scattered electron (BSE) and secondary electron (SE) emissions stimulated by the focused electron beam. Figure 8 shows a secondary electron contrast image formed using the SE detector. In this image contrast is associated with the topography of the surface, deliberately introduced by thermal grooving.

***4.b.i. Image Processing; Edge Detection.*** Contrast images are analyzed by the Image Processing module in order to extract geometrical information about the location and geometry of interfaces. A central component of this module is edge detection. It is known that gradients in the intensity contrast images are often associated with interfaces. The intensity signature of these gradients, however, varies widely depending upon the type of contrast image formed and the preparation of the sample surface. Thus, the Image Processing

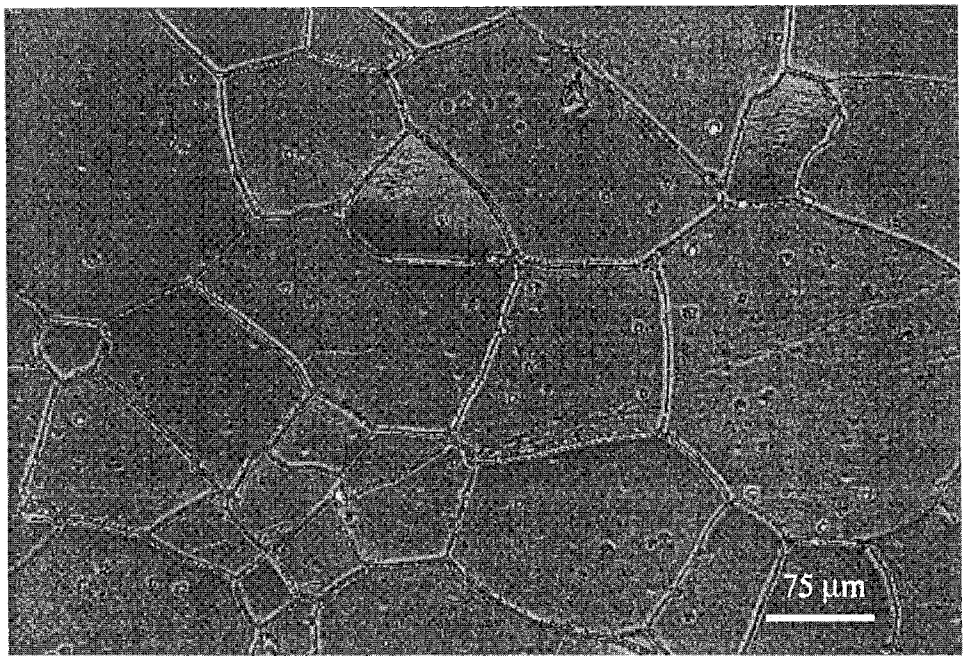


*Figure 8.* A secondary electron contrast image of MgO showing grain boundary contrast from thermal grooving.

function requires a broad range of algorithms with sufficient flexibility to be effective in locating interfaces from a variety of contrast images.

For line boundaries, as observed for oxide surfaces with grooved boundaries, several approaches have been developed, including the use of two Gabor filters and median filters [27, 28]. Other methods used to assist in edge detection include various combinations of Gaussian smoothing, noise reduction using median filters, blob coloring and morphological erosion (plus dilation) to remove isolated artifacts such as precipitates, pits, etc. [29]. The selection of a particular approach to Image Processing is a matter of experience and selection from among the set of available algorithms and is highly material dependent.

***4.b.ii. Image Processing: Skeletonization.*** After successful detection of edges in the image, the image is thresholded to obtain a binary image. This image is then subjected to morphological filters which reduce it to a "skeletonized" form, in which each line is only one pixel wide. The skeletonized image for Fig. 8 is shown by superposition in Fig. 9. Spurious boundary segments or "spurs" that occur in the skeletonized image are also removed.

The connectivity of the skeletonized image is analyzed to locate the triple junctions. From the identified coordinates of the triple junctions, the electron probe is directed (by beam deflection using the magnetic lens system of the SEM) to specific points near the junctions. These points are obtained by first applying a line-following routine to the skeletonized image to find the location of each identified triple junction, and then by further locating a set of three points lying in the interiors of the three associated grains at each junction. It should be clear that the auxiliary points required to characterize the triple junction derive from a knowledge, not only of the location of the triple junction, but also of the geometrical location (inclination) of each grain boundary associated with that junction.

***4.b.iii. Orientation Indexing.*** The final steps associated with MIMS in the sector include the positioning of the beam at each identified point, the collection of an EBSP there, followed by the indexing of each EBSP to determine local lattice phase and orientation. These operations are associated with the Automatic EBSP Indexing module. The indexing function of MIMS does not differ from conventional OIM. The main ideas associated with pattern indexing have been described previously [30].

### *4.c. Systems Control*

Sequencing and control of the operations of MIMS is provided by the Systems Control module. When

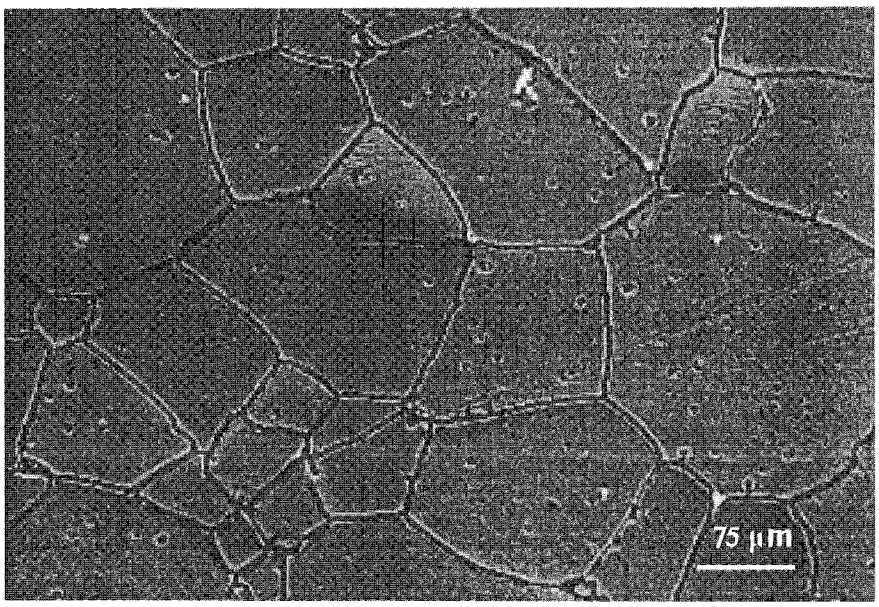


*Figure 9.* The skeletonized boundaries are shown superimposed onto Fig. 8 as black curves; not all boundaries are skeletonized.

multiple sectors are required, the Systems Control module directs the Microscope module to change position of the mechanical stage to the next sector, and the complete process is repeated again. Repetition continues until sufficient sectors have been acquired. Stitching of these sectors to form a wide-field 2-D image is accomplished by a separate algorithm which makes use of the mean square error of the correlation of the overlapping images to obtain the translations and rotations needed to bring the adjacent images into the best possible registry. From Fourier transforms of the overlap region, the shape of the correlation peak is known. Based on several samples, the registration can be obtained to sub-pixel accuracy.

### *4.d. 3-D Reconstruction*

The electron opacity of most crystalline materials provides a serious challenge to the complete characterization of the interfacial network. Full characterization of interfaces requires information about the inclination of the interfacial plane. Likewise, the full characterization of triple junctions requires the description of the orientation of the junction line itself. These data are inaccessible in a single-section characterization of the network. Three-dimensional reconstruction here refers to registry between the data upon any of the adjacent section planes obtained by calibrated (parallel) serial sectioning.

We consider that the points $x$ associated with features in a specified 2-dimensional section represent their "reference positions", and that the associated "variable positions" in the adjacent section plane are given by $y$. The relationship between reference and variable positions must be given by the rigid body rotation, $O$, and the translation vector, $t$, according to the expression

$$y = Ox + t. \tag{4.2}$$

It is assumed that the component of the translation vector perpendicular to the section plane is a known constant. It is also assumed that an exact correspondence the selected features common to both planes is known.

Generally, several (or many) feature points (e.g. boundaries, triple points, indentations) are measured in their reference and variable positions. It is then assumed that each point must be related in its reference and variable positions by the same $(O, t)$ transformation. Thus

$$y_i = Ox_i + t \; (i = 1, 2, \ldots, N), \tag{4.3}$$

where $N$ is the number of feature points determined from the data. Due to experimental errors, relations (4.3) are only approximate, and a best fit for the transformation $(O, t)$ must be obtained by the minimization of the function

$$\psi = \sum_i \omega_i (y_i - (Ox_i + t))^2, \tag{4.4}$$

where $\omega_i$ is a non-negative weight assigned to the $i$th feature point.

There is an inherent physical assumption in the minimization problem expressed by Eq. (4.4). It is that there is no directional anisotropy present in the set of feature points examined by the analysis. For example, if common triple junctions are used as feature points, the present analysis assumes that the triple junctions are randomly distributed in all directions. In cases where this assumption is invalid, the character of the distribution must be known in order to conduct the registry analysis.

The minimization problem posed in Eq. (4.4) is one which has been widely applied for many years in various fields. The solution for the translation vector is given as the difference between the centroids of true and incorrect points according to the expression

$$t = \frac{(\sum_i \omega_i (y_i - Ox_i))}{\sum_j \omega_j}. \tag{4.5}$$

The rotation $O$ is obtained from the polar decomposition of a certain matrix constructed from the $x_i$ and $y_i$ vectors [31].

Two approaches have been taken in connection with the aforementioned analysis; these can also be combined. The first approach involves the use of "external markers" which are in common between any two adjacent section planes. A common example is the use of several hardness indentations which are observable on both planes. The centroid of the matching pairs of indentations on each plane can be used as the true and incorrect positions in Eq. (4.5). The problem with external markers is associated with the fact that these markings are typically quite large relative to the features of interest in the microstructure. Determination of a precise location of the centroid of these features can be problematical, and thus errors can be large.

When precise registry between adjacent section planes is necessary, it is useful to employ "internal markers". These are features of the microstructure itself that carry over from one section plane to the next.

Examples include the orientations and phases of the grains themselves, the positions of triple junctions and grain boundaries, twin boundaries, etc. Usually the use of internal markers requires one or more additional assumptions about the statistical nature of the distribution of these markers in the microstructure. For example, it might be assumed that the orientation distribution of the triple junctions is uniform (i.e., there is no preferred direction to the distribution of triple lines in the microstructure). The measured distribution can then be compared with the uniform model distribution (with its associated geometrical weighting factors $\omega_i$) through Eq. (4.5). In some instances (e.g., when twin boundaries are present in the microstructure) additional statistical assumptions may not be necessary.

The typical approach used in connection with MIMS is a two-step process. First, external markers are employed to achieve a coarse registry between sections. Then, a selected set of internal markers is used to refine the registry.

## 5. Results

### 5.a. *Relative Grain Boundary Energies in Magnesia*

***5.a.i. The Sample.*** Magnesia powder was formed by decomposing 99.7% pure magnesium carbonate (Fisher Scientific) at 997°C in air. Uniaxial compaction in a hot press at 1700°C for one hour at 61 MPa produced a disc with a diameter of 50 mm and an average thickness of 1.5 mm. Specimens cut from this disc were then packed in a magnesia crucible with the parent powder and annealed for 48 h at 1600°C in air. At the end of this treatment, the specimens were translucent. Surfaces were prepared using an automatic polisher (Logitech PM5). The surfaces were initially lapped with a 9 micron alumina slurry and the final polish was achieved using an alkaline (pH ~10) colloidal silica (0.05 micron) slurry. The flatness of the final surface was measured using an inductive axial movement gauge head with a resolution of 0.1 $\mu$m. (Brown and Sharpe, TESR, Model TT22); surfaces were determined to be flat within $\pm 0.3$ $\mu$m over lateral dimensions of 1 cm. The surface was thermally grooved by annealing it in air for 5 h at 1400°C. The average grain size of the sample was 109 $\mu$m and the average groove width was 2.4 $\mu$m. At this stage, one sample was analyzed for impurities by atomic absorption. The sample contained 0.2% Ca, 0.02% Al, 0.03% Fe, 0.02% Si, and 0.03% Y.

***5.a.ii. Data Acquisition.*** The microstructure was characterized using the MIMS system. Orientations were determined from electron backscattered diffraction patterns (EBSPs); dihedral angles at each triple junction were determined based on lines fit to the boundary contrast in secondary electron images. A $3.7 \times 12.4$ mm area of the sample was probed and from this region 4665 boundaries associated with 1555 triple junctions were characterized; this is approximately 40% of the triple junctions in the analyzed area. After analysis, $6.2 \pm 0.3$ $\mu$m was removed by polishing and the thermal grooving treatment was repeated. Secondary electron images were recorded over the same area so that the boundary inclinations with respect to the sample surface plane and true dihedral angles could be determined.

***5.a.iii. Results for Grain Boundary Energies.*** Figure 10 shows a portion of the raw data which are plotted in Rodrigues-Frank space [19]. For simplicity, only the segment for which $0 \leq R_3 < 0.037$ is shown. Each observed disorientation is plotted as a

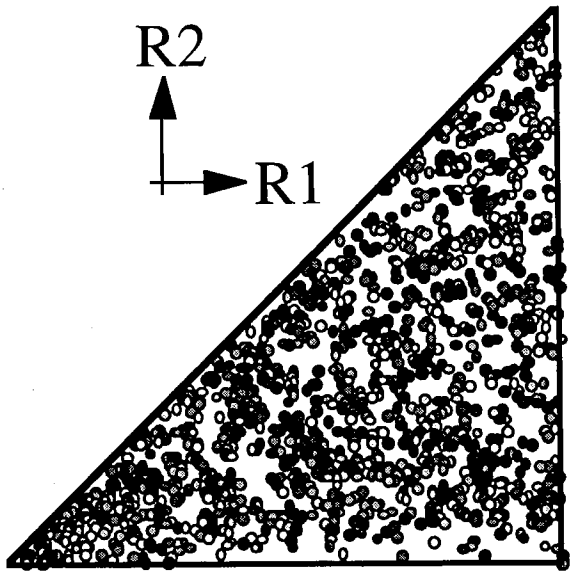


*Figure 10.* (a) Observed dihedral angle distribution in Rodrigues-Frank space; only points for which $0 \leq R_3 < 0.037$ are shown. Each observation is shaded according to the size of the dihedral angle where the lightest shades are equal to 146° and the darkest to 98°. Misorientations based on ⟨100⟩ axes occupy the lower edge of the triangle, and ⟨110⟩ misorientations occupy the hypotenuse. (b) The values of the best fit function for the grain boundary energy, at each of the observed disorientations, in the same region of Rodrigues-Frank space. Here, the lightest shade equals 1.24 and black is zero.

point in the space (in many cases the points overlap one another) and each point is shaded according to the dihedral angle observed opposite each boundary. The lightest points correspond to the highest dihedral angles ($\chi_{max} = 180°$) and the darkest points to the smallest dihedral angles ($\chi_{min} = 30°$). There is a cluster of points with the highest dihedral angle near the origin where there is the smallest disorientation. For all measurements, the median of the dihedral angle distribution was 121.6° and the standard deviation of the distribution was 24.1°.

The data for true dihedral angles, together with the orientation information were analyzed by means of the statistical/multiscale method described above. The boundary condition was imposed of zero grain boundary energy for zero misorientation, i.e. at the origin of Rodrigues space. Use of this boundary condition required the use of cells centered on zero. Although by the a 3 by 3 by 3 discretization and a $5 \times 5 \times 5$ grid were used to construct the energy function, the limited data set was such that only the results from the $3 \times 3 \times 3$ grid are shown here. Figure 11 shows a plot of the variation in grain boundary energy with misorientation for the three primary edges of Rodrigues space, i.e. misorientations based on rotations about ⟨100⟩, ⟨110⟩ and ⟨111⟩. The results suggest that the energy is highest along ⟨111⟩ though lower at the twin position. The energy appears to rise along ⟨110⟩ monotonically whereas it as nearly constant along ⟨100⟩, apart from low angle boundaries.

***5.a.iv. Discussion of Grain Boundary Energy Results.*** The broad features of both the raw data and of the fit function reproduce expectations. Specifically, the boundaries with the smallest disorientations have the largest measured dihedral angles and, according to the fit grain boundary energy function, the lowest energy. One might expect to observe cusps in the energy at certain special boundaries representing low Σ CSL disorientations. However, the width of such a cusp is only expected to be on the order of $15°(\Sigma)^{-1/2}$ [21]. This energy resolution condition excludes all but the Σ3 orientation which appears as a broad minimum at the end of the ⟨111⟩ series of disorientations.

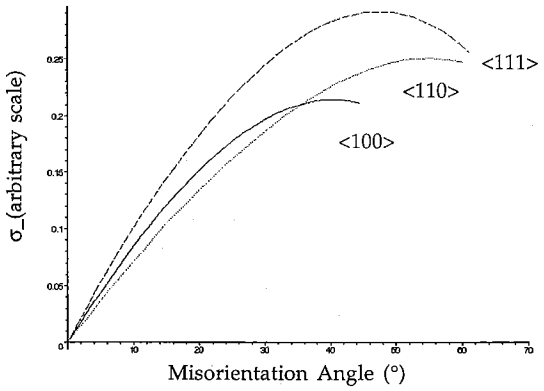


*Figure 11.* Variation of Grain Boundary Energy (on an arbitrary scale) with misorientation for the three low index zones, ⟨100⟩, ⟨110⟩ and ⟨111⟩.

The result that grain boundary energies appear to be higher along ⟨110⟩ than along ⟨100⟩ is an agreement with the measurements of Dhalenne et al. [8] obtained from thermal groove measurements. These experimental results are subject to uncertainty because they are simply ratios between grain boundary energies and an assumed constant surface energy. With the assumption of constant surface energy, the energies of symmetric ⟨110⟩ tilt boundaries are everywhere higher than those of ⟨100⟩ boundaries, except at the (coherent) twin position. If the surface energies vary with inclination, see below, then there may need to be some adjustment of Dhalenne's results.

### *5.b. Surface Energies in Magnesia*

Several testbed simulations with artificial data have shown the multiscale analysis method discussed in Section 3.f above to be robust and efficient. Implementation may be rather complicated since, in general, the independent parameters must be referred to crystallographic coordinates, or some other coordinate frame. Given the number of possible variables, in general 5 independent parameters, it is important to seek situations where some may be ignored, similar to the example above.

***5.b.i. Thermal Groove Measurement: Reconstruction of Surface Energy.*** Rohrer and Saylor [32, 33] measured the geometry of thermal grooves for a number of island grains in an MgO polycrystal with the objective of measuring surface energy anisotropy. This experiment permitted certain key aspects of the multiscale reconstruction method to be explored. MgO has a rock salt structure, which can be regarded as having an fcc lattice of anions with cations occupying all the octahedral interstices. The relevant microstructural features are small occluded grains each of which is surrounded by a larger grain. The lattice misorientation

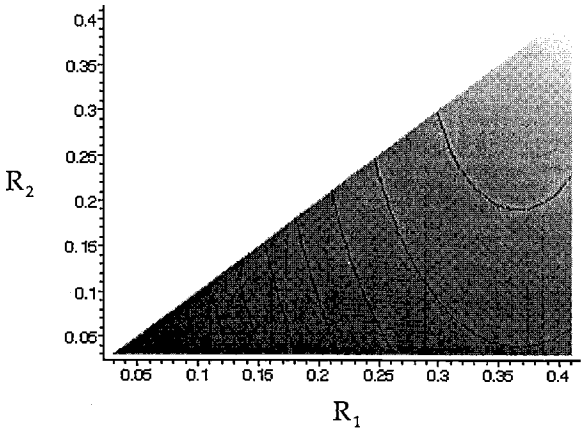


*Figure 12.* Contour plot of the grain boundary energy with $R_3 = 0.05$. The energy is zero at the origin (zero misorientation), increases monotonically with increasing misorientation and then decreases towards the right edge of the section.

between any occluded grain and its surrounding grain is small, i.e. no more than a 10° disorientation angle. The surface energy, rather than the grain boundary energy, may be ascertained as a function of normal direction by characterization of the thermal grooves bounding the islands. With only eight grains and several dozen thermal groove profile geometries measured around each grain perimeter for a total of about 400 triple junctions, the experimental data set is small. It is also poorly distributed; there is a data island near (100). The reconstruction, Fig. 12, stops at level $L = 4$, or a $16 \times 16$ mesh. One unsuspected feature of the data set is that the equations relating the solution near the (111) directions of the surface normal are not connected to directions distant to (111), rendering the reconstructed solution very approximate near this direction.

The reconstructed surface energy, $\sigma$, satisfies

$$\frac{\sigma(111)}{\sigma(100)} = 1.11, \frac{\sigma(110)}{\sigma(100)} = 1.08, \text{ and}$$
$$\sigma(100) < \sigma(110) < \sigma(111),$$

consistent with the coordination numbers of the (100), (110), and (111) planes in a rock salt structure. That is to say, the number of bonds that must be broken per atom are one, two and three for the (100), (110) and (111) surfaces, respectively. Converting these to boroken bond densities per unit are and disregardning relaxation effects, the expected ranking is the same as that observed, i.e. $\sigma(110)/\sigma(100) = \sqrt{2}$ and $\sigma(111)/\sigma(100) = \sqrt{3}$. The variation of the surface

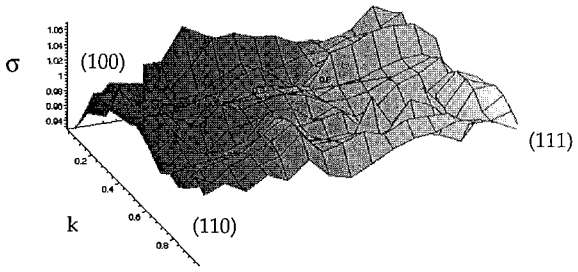


*Figure 13.* Plot of the excess free surface energy, $\sigma$, for MgO, plotted (on an arbitrary scale) as a function of the Miller index coordinates $(h, k, l)$ with $h = 1, 0 \le k \le 1, 0 \le l \le 1$.

energy falls in the expected range; see [32] for a discussion of the stability of surface orientation or faceting in MgO. Note also that the surface energy is largest near (111) but actually decreases slightly as one approaches the (111) position. A smoother version of the surface energy variation is presented in Fig. 13, where a Fourier function has been interpolated to the discrete data in the reconstruction. Even in the smoothed form, there is a range of approximately 10% in surface energy.

***5.b.ii. Reconstruction of Surface Energy: Role of Torque Terms.*** One of the most significant conclusions that to be drawn from this analysis is the role of the torque terms in the reconstruction of the syrface energy, cf. Fig. 12. The Herring Relations, Eq. (2.1), arise as the natural boundary conditions for equilibrium of a grain boundary system meeting on a triple line, (or at a triple point in a two-dimensional system). If $\sigma$ is not constant as a function of normal angle $\theta$, then torque terms must be present to maintain equilibrium on the triple line. In particular, since the excess free surface energy of MgO is not constant, it depends on the normal direction. Even so, one may be tempted to believe that the influence of the torque terms is extremely small, and thus be led to neglect them in the reconstruction of the energy. Figure 14 gives a graphical comparison of two reconstructions, the one obtained with torque terms included (as in Fig. 12) and another one reconstructed neglecting the torque terms. The result is striking: The data structure of reconstructed values without torque terms has a higher mean and a standard deviation of 0.161 whereas the reconstruction with torque terms has a standard deviation of 0.025.

## 6. Summary & Conclusions

The development of a systematic approach to extracting grain boundary energies from geometrical and

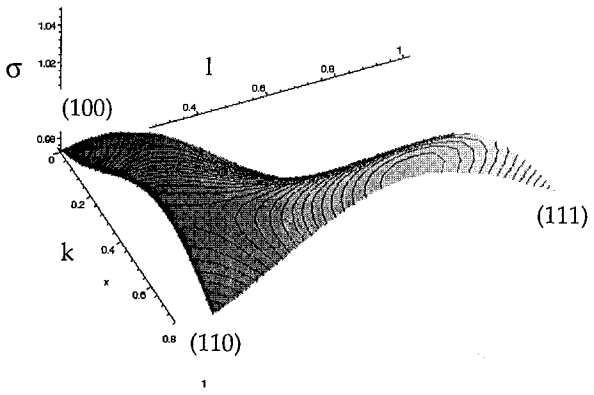


*Figure 14.* Plot of the excess free surface energy for MgO, plotted (on an arbitrary scale) within the unit triangle with $h = 1, 0 \leq k \leq 1$, $0 \leq l \leq 1$. The smooth surface is a Fourier series interpolation based on the discrete reconstruction shown in the previous figure.

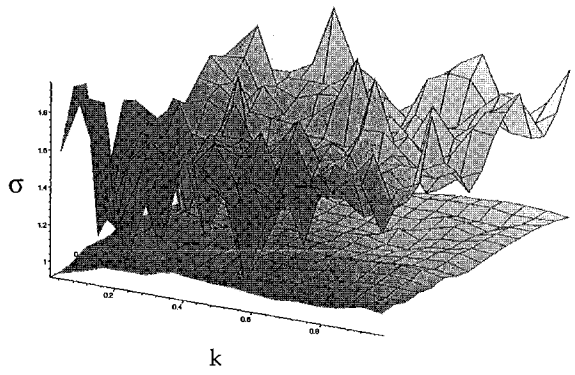


*Figure 15.* Plot of the reconstructed surface energy (on an arbitrary scale) for MgO assuming either negligible torques (upper surface) or including torque terms (lower surface, cf. Fig. 13). The results suggest that inclusion of torque terms leads to a more accurate result.

crystallographic information on the microstructure has been outlined. The approach relies on the assumption of local equilibrium at triple junctions between grain boundaries or between a grain boundary and a surface which permits the application of Herring's relations as equalities on a force balance. The circumstances under which such an approach is justified is summarized with respect to cusps in the energy distribution and triple line drag. Application of a statistical/multiscale analysis to large data sets is described. Examples are given for analysis of grain boundary energies and surface energies in magnesia, based on triple junction geometry and thermal groove geometry, respectively. The results illustrate that useful information can be obtained in this manner. They also hint at the importance of the dependence of grain boundary energy with inclination, and hence of the torque terms in the Herring equations.

## Acknowledgments

This work was supported primarily by the MRSEC Program of the National Science Foundation under Award Number DMR-9632556. DK and DEM were also supported by the Army Research Office under Award Number DAAH04-96-10060 and the National Science Foundation under Award Number DMS-9505078. ST was also supported by the National Aeronautics and Space Administration under NASA Grant No. NAG-1666.

## References

1. D. Vaughan, Acta Metall. **16**, 563 (1968).
2. G. Palumbo, E.M. Lehockey, and P. Lin, JOM **50**, 40 (1998).
3. A.D. Rollett and W.W. Mullins, Scripta Metall. et mater. **36**, 975 (1996).
4. B.L. Adams, D. Kinderlehrer, W.W. Mullins, A.D. Rollett, and S. Ta'asan, Scripta Mat. **38**, 531 (1997).
5. C. Herring, Phys. Rev. **82**, 87 (1951).
6. A.P. Sutton and R.W. Balluffi, *Interfaces in Crystalline Materials* (Clarendon Press, Oxford, UK, 1995).
7. N.A. Gjostein and F.N. Rhines, Acta Metall. **7**, 319 (1959).
8. G. Dhalenne, M. Dechamps, and A. Revcolevschi, in *Advances in Ceramics*, vol. 6 (American Ceramic Society, Columbus, OH, 1983), p. 138.
9. A. Otsuki, Mater. Sci. Forum **207–209**, 413 (1996).
10. A. Otsuki, H. Yato, and I. Kinjyo, Mater. Sci. Forum **126–128**, 285 (1993).
11. C. Herring, in *The Physics of Powder Metallurgy*, edited by W.E. Kingston (McGraw-Hill Book Co., New York, 1951), p. 143.
12. J.W. Gibbs, in Collected Works (Dover, New York, 1961), p. 56.
13. E. Fermi, *Thermodynamics* (Dover, New York, 1937).
14. W.W. Mullins, in *Metal Surfaces: Structure, Energetics and Kinetics* (ASM, Cleveland, OH, City, 1962), p. 17.
15. V.E. Fradkov and D. Udler, Adv. Physics **43**, 739 (1994).
16. V. Randle, *The Role of the Coincidence Site Lattice in Grain Boundary Engineering* (Institute of Materials, London, UK, 1996).
17. U.F. Kocks, C. Tomé, and H.-R. Wenk (eds.), *Texture and Anisotropy* (Cambridge University Press, Cambridge, UK, 1998).
18. H. Bunge, *Texture Analysis in Materials Science* (Butterworths, London, 1982).
19. F. Frank, Met. Trans. **19A**, 403, (1988).
20. V. Randle, *Microtexture Determination and its Applications*, (The Institute of Materials, London, 1992).
21. D.G. Brandon, Acta Metall. **14**, 1479 (1966).
22. M.L. Kronberg and F.H. Wilson, Trans. Met. Soc. AIME **185**, 501 (1949).
23. W. Bollmann, *Crystal Defects and Crystalline Interfaces*, (Springer Verlag, New York, 1970).

24. D. Wolf and J.F. Lutsko, Z. Kristallogr. **189**, 239 (1989).
25. M. Takashima, A.D. Rollett, and P. Wynblatt, Phil. Mag. A. (1999), submitted.
26. S.I. Wright, J. Comp. Assist. Microscopy **5**, 207 (1993).
27. H.-C. Chao, Trans. ASM **60**, 37 (1967).
28. R.N. Wright, Met. Trans. **3**, 83 (1972).
29. H.-C. Chao, Met. Trans. **4**, 1183 (1973).
30. B. Adams, K. Kunze, and S.I. Wright, Met. Mater. Trans. **23A**, 819 (1993).
31. A. Morawiec and D. Saylor, in ICOTOM-12, Montreal, Canada, City, NRC Research Press, Ottawa, Canada **1**, 198 (1999).
32. D.M. Saylor, D.E. Mason, and G.S. Rohrer, J. Am. Ceram. Soc. submitted.
33. D.M. Saylor and G.S. Rohrer, J. Am. Ceram. Soc. **82**, 1529 (1999).